Adsorption-induced multiple magnetic phase transitions in monolayer MPX_3 (M = V, Mn; X = S, Se, Te)

Dong Liu, Sike Zeng, Jihai Liao, Yao Yao, and Yu-Jun Zhao[*]
Department of Physics, South China University of Technology, Guangzhou 510640, China

(Received 3 December 2025; revised 7 April 2026; accepted 5 May 2026; published 1 June 2026)

Modulating magnetism in two-dimensional (2D) materials is of great importance for the development of spintronics. Although surface adsorption has been demonstrated as an effective approach for tuning electronic and magnetic properties, its application in 2D magnetic materials is still emerging. In this work, we demonstrate that surface adsorption can robustly induce multiple magnetic phase transitions in Néel antiferromagnetic MPX_3 monolayers. By selectively adsorbing representative metal (Be, Ca) and highly electronegative nonmetal (O, F) atoms on MPX_3 with their corresponding energetically favored configuration, the antiferromagnetic ground state can be transformed into ferromagnetic, altermagnetic, ferrimagnetic, or fully compensated ferrimagnetic states, accompanied by significant nonrelativistic spin splitting. Specifically, adsorption of highly electronegative atoms (such as O and F) breaks the symmetry between opposite spin sublattices, leading to altermagnetism in VPX_3, characterized by nonrelativistic spin splitting in the band structure and a symmetry-protected zero net magnetization. In $MnPX_3$, adsorption of electronegative atoms induces a semiconductor-to-half metal transition, and drives an antiferromagnetic-to-ferromagnetic transition. For metal atom adsorbates (e.g., Be, Ca), their favorable configurations break all symmetries connecting opposite spin sublattices, resulting in ferrimagnetic spin splitting in MPX_3. When the system remains gapped, appropriate band filling ensures fully compensated magnetization. Our findings provide valuable guidance for designing high-performance spintronic devices based on monolayer MPX_3.

DOI: 10.1103/lgdz-961s

I. INTRODUCTION

Conventional studies of collinear magnetism have primarily focused on ferromagnets and antiferromagnets. In ferromagnets, all magnetic moments align parallel to each other, resulting in a nonzero net magnetization and spin splitting in the electronic band structure. In contrast, in conventional antiferromagnets (cAFMs), the magnetic moments adopt an antiparallel arrangement, leading to a vanishing net magnetization protected by symmetry and spin-degenerate bands. Traditional spintronics has largely relied on ferromagnets, yet their unavoidable stray fields impose stringent limits on storage density and device scalability. Compared to ferromagnets, antiferromagnets offer several advantages, such as high robustness against external magnetic fields, absence of stray fields, and ultrafast spin dynamics. However, cAFMs generally lack strong spin-current responses and exhibit no breaking of time-reversal symmetry, which restricts their potential for certain applications [1].

Recent research focus has shifted toward novel magnetic phases that combine the advantages of both ferromagnetic (FM) and conventional antiferromagnetic (AFM) systems, holding great potential for next-generation spintronic devices. Among them, a phase termed "altermagnetism" has been proposed, characterized by a symmetry-protected zero net magnetic moment and momentum-dependent spin splitting [2]. Its unique electronic structure enables a range of emergent phenomena, such as spin-polarized currents, crystal thermal properties, the crystal Hall effect, Kerr effect, and giant magnetoresistance, underscoring its promising prospects for spintronic applications [3–12]. In parallel, fully compensated ferrimagnets (fFIMs) exhibiting nonrelativistic spin splitting have also attracted considerable attention [13]. In altermagnets (AMs), the zero net moment is safeguarded by spin group symmetry, whereas in fFIMs, it is stabilized by appropriate band filling. However, studies on two-dimensional (2D) AMs and fFIMs remain largely uncharted. In particular, clear experimental evidence for fFIMs and AMs is still elusive. Since the experimental realization of 2D CrI_3 [14] and $Cr_2Ge_2Te_6$ [15] in 2017, magnetic van der Waals materials with exceptional tunability have garnered significant interest, opening new pathways for exploring low-dimensional magnetism.

Meanwhile, the family of transition metal phosphorus trichalcogenides (MPX_3) in their monolayer form, has attracted significant interest due to their ability to sustain a long-range magnetic order in the 2D limit. Bulk $MnPSe_3$ was synthesized as early as 1981 and was observed to exhibit a Néel-type AFM ground state [16]. Over the past decade, studies have largely centered on the effects of strain and doping on monolayer MPX_3 [17–21]. In recent years, with the emergence of altermagnetism, efforts have shifted toward achieving this magnetic phase in MPX_3 systems via the application of vertical electric fields and the construction of Janus structures [22,23]. Additionally, the valley degree of freedom near the Fermi level, constrained by symmetry, has been

---

[*] Contact author: zhaoyj@scut.edu.cn

actively tuned in these materials. Theoretical calculations have further corroborated the realization of the anomalous valley Hall effect (AVHE) in such engineered structures [24,25].

In this work, we systematically investigate the electronic and magnetic properties of adsorption-regulated monolayer MPX_3 (M = V, Mn; X = S, Se, Te) using first-principles calculations. The pristine MPX_3 monolayer exhibits a Néel-type antiferromagnetic ground state. By adsorbing different atomic species on the surface of MPX_3, we successfully engineer a variety of magnetic phases, including unconventional nonrelativistic spin-split states—such as the altermagnetic (AM) and fully compensated ferrimagnetic (fFIM) phases.

II. COMPUTATIONAL DETAILS

Our first-principles calculations are performed using the Perdew-Burke-Ernzerhof (PBE) generalized gradient approximation (GGA) [26], as implemented in the Vienna *Ab Initio* Simulation Package (VASP) [27]. The plane-wave basis set is truncated at a kinetic energy cutoff of 500 eV. To minimize spurious interactions between periodic images, a vacuum layer of 20 Å is introduced along the z direction in the slab model. Sampling of the Brillouin zone is carried out using Monkhorst-Pack k-point grids: a $9 \times 9 \times 1$ mesh for the $1 \times 1 \times 1$ unit cell and a $4 \times 4 \times 1$ mesh for the $2 \times 2 \times 1$ supercell of MPX_3. During geometry optimization, all internal atomic positions are fully relaxed until the Hellmann-Feynman forces on each ion are below 0.01 eV Å^{-1} and the total energy is converged within 10^{-6} eV. Spin-orbit coupling (SOC) is applied in the calculations of magnetic anisotropic energy (MAE) [28,29]. Phonon calculations were performed using the PHONONBENCH code [30–33]. For the evaluation of magnetic properties, an effective Hubbard U correction is applied to the $3d$ electrons of Mn and V atoms, with values of $U = 5$ and 3.25 eV, respectively, following previous references [19,34]. The Néel and Curie temperatures were simulated using the VAMPIRE atomistic simulation software package [35]. The adsorption energy E_{ad} was calculated using the following equation:

$$E_{\text{ads}} = E_{\text{total}} - E_{\text{sub}} - E_{\text{atom}}, \tag{1}$$

where E_{total}, E_{sub}, and E_{atom} represent the total energies of the adsorbed atom on MPX_3, the pristine MPX_3 substrate, and the isolated impurity atom, respectively. The chemical potentials of constituent elements are calculated by referencing their stable bulk or molecular phases. For monolayer MPX$_3$, we set μ_M, μ_P, and μ_X relative to the total energies of bulk M, bulk P, and bulk X (or X_2 molecule), respectively, with the formation energy $\Delta H_f = E_{2\text{D}} - \mu_M^0 - \mu_P^0 - 3\mu_X^0$. The actual chemical potentials are $\mu_i = \mu_i^0 + \Delta\mu_i$, where $\Delta\mu_i \leqslant 0$ and the $\Delta\mu_i$ satisfy $\Delta\mu_M + \Delta\mu_P + 3\Delta\mu_X = \Delta H_f$. Competing phases are excluded by imposing $a\Delta\mu_M + b\Delta\mu_P + c\Delta\mu_X \leqslant \Delta H_f^{\text{comp}}$ for any M$_a$P$_b$X$_c$ compound. This approach yields the thermodynamically allowed chemical potential window for the 2D phase.

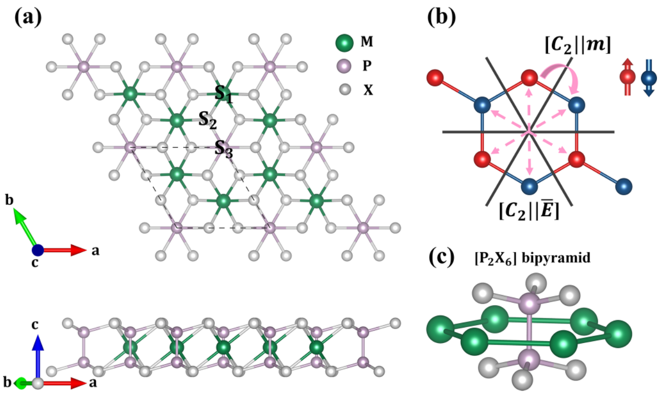

FIG. 1. (a) Top and side views of the monolayer MPX_3 structure, with top sites S_1 (above the M atom), S_2 (above the X atom), and S_3 (above the P atom) indicated. (b) The spatial inversion symmetry P and mirror symmetry m connect sublattices with opposite spins in the NAFM state. (c) A honeycomb lattice of M atoms encloses the $(P_2X_6)^{4-}$ bipyramidal units.

III. RESULTS AND DISCUSSION

A. Structure and surface adsorption considerations of pristine MPX_3

Prior to investigating the adsorption of impurity atoms on MPX_3 surfaces, it is essential to examine the structural and magnetic properties of monolayer MPX_3. Fig. 1(a) present the top and side views of the crystal structure, respectively, where the unit cell is outlined by the black dashed lines. Each unit cell contains two M atoms, two P atoms, and six X atoms. The atomic structure of monolayer MPX_3 is stabilized by $(P_2X_6)^{4-}$ bipyramids arranged in a triangular lattice, which form coordination sites for the transition-metal ions, as illustrated in Fig. 1(c). The corresponding space group is P$\bar{3}m1$.

To determine the magnetic ground state of pristine MPX_3, we considered four magnetic configurations: ferromagnetic (FM), stripy antiferromagnetic (SAFM), Néel antiferromagnetic (NAFM), and zigzag antiferromagnetic (ZAFM), as depicted in Fig. S1 (see Supplemental Material (SM) [36] for more details). The magnetic unit cells for the FM and NAFM states are identical to the structural unit cell (1×1). For the SAFM and ZAFM states, however, the magnetic periodicity necessitates a larger cell; we therefore employ a rectangular 2×2 supercell to model these magnetic orders. Our calculations reveal that the magnetic ground state of MPX_3 is NAFM (see Table S1 in SM [36]), consistent with previous studies [17,19]. Accordingly, the spin point group of MPX_3 is ${}^2\bar{3}{}^2m$. The symmetries connecting opposite spin sublattices primarily include spatial inversion P and mirror reflection m, as shown in Fig. 1(b), indicating that MPX_3 is a PT-type antiferromagnet.

Therefore, in these systems, the key to realizing the first type of unconventional magnetic phase, altermagnetism, lies in breaking the P symmetry that protects the spin degeneracy of the energy bands, while preserving the mirror symmetry m [37]. In contrast, realizing the second type of unconventional magnetic phase (fully compensated ferrimagnetism) is relatively more straightforward. It generally requires that adsorption renders the two spin sublattices inequivalent and

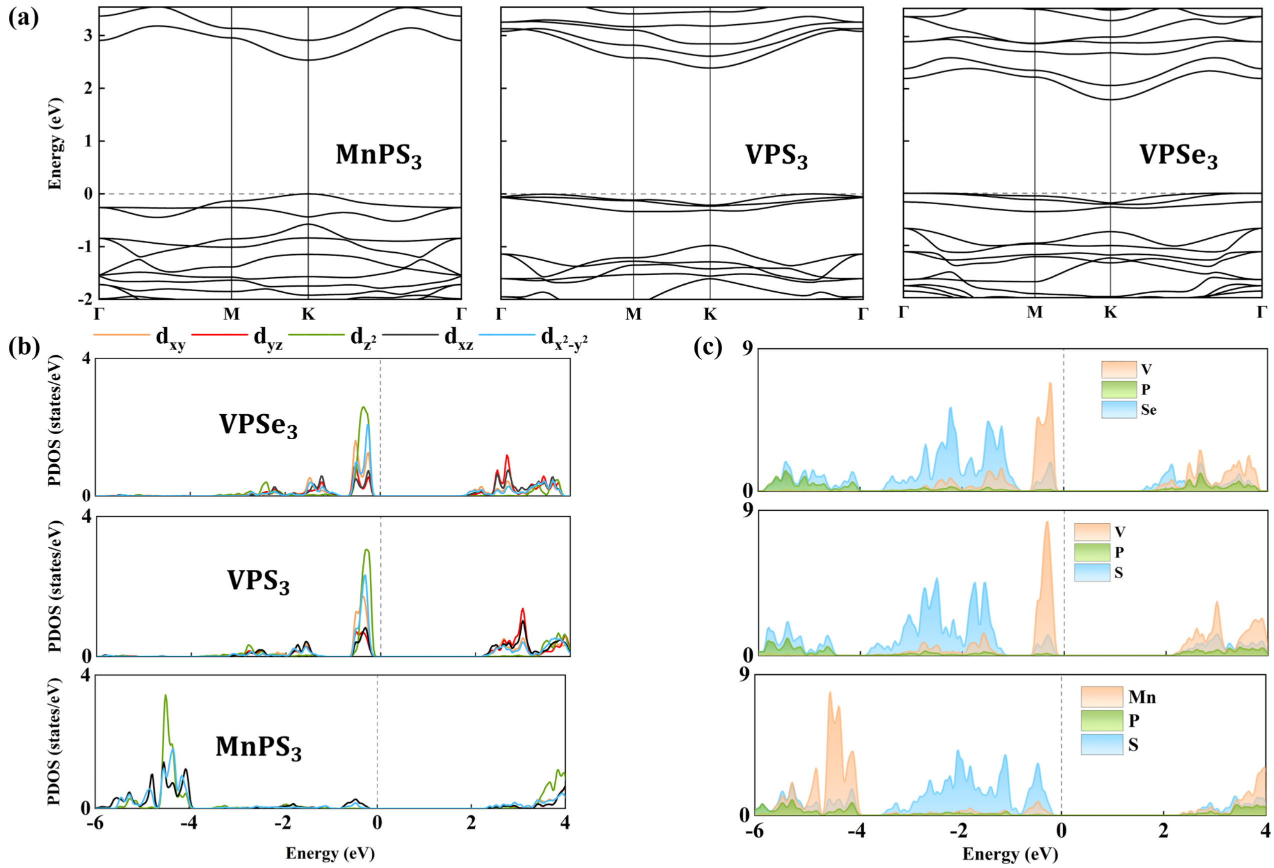

FIG. 2. (a) Calculated PBE + U band structures of $MnPS_3$, VPS_3, and $VPSe_3$ monolayers in their ground states. (b) Projected density of states (PDOS) onto the $3d$ orbitals of the transition metal M in the MPX_3 monolayer. (c) PDOS for M, P, and X atoms in the ground state.

maintains the semiconducting band gap of MPX_3, invariably leading to the formation of a fully compensated ferrimagnet.

Three adsorption sites are considered, labeled S_1 (above the M atom), S_2 (above the X atom), and S_3 (above the P atom), as illustrated in Fig. 1(a). Notably, the S_1 site does not lie on any symmetry element, whereas the S_3 site sits on a mirror plane, and the S_2 site resides simultaneously on both a mirror plane and a rotational axis. We further examined the adsorption of metallic elements (such as Li, Na, and Ca) and highly oxidative elements (such as O, F, and Cl). Our calculations reveal that reducing metal elements generally prefer adsorption at the S_1 site, while oxidizing elements tend to adsorb at the S_3 site. Additionally, we find that under certain conditions, such as O or F adsorption on $MnPX_3$ surfaces, the system can transition from a semiconductor to a half-metal or metal. In such scenarios, this electronic transition is accompanied by an AFM-FM phase transition.

For clarity, we present in the main text one representative case for each system to illustrate how surface adsorption enables diverse magnetic phases in MPX_3, while additional analogous adsorption scenarios and corresponding computational results are provided in Ref. [36]. The selected examples include the following: O adsorption on $VPSe_3$ to unlock altermagnetism, F adsorption on $MnPS_3$ inducing an AFM-FM transition, and Be adsorption on VPS_3 realizing a fFIM state. Furthermore, we evaluate the dynamical and thermodynamic stability of each adsorption configuration to assess the feasibility of experimental synthesis and provide a detailed analysis of the electronic and magnetic properties before and after adsorption.

B. Electronic and magnetic properties of monolayer MPX_3

We first calculated the electronic band structures of the pristine single-layer MPX_3 compounds. The band structure plots for $VPTe_3$, $MnPSe_3$, and $MnPTe_3$ are provided in Ref. [36] (see Fig. S4), while the band structures of $VPSe_3$, $MnPS_3$, and VPS_3—which serve as representative cases demonstrating the three distinct magnetic phase transitions induced by adsorbed adatoms—are presented in Fig. 2. Our results reveal that $MnPX_3$ are direct-gap semiconductors, whereas VPX_3 exhibit indirect band gaps. Notably, the band gap of $MPTe_3$ is substantially narrower than those of MPS_3 and $MPSe_3$, with MPS_3 possessing the largest gap (Table I). Furthermore, the electronic bands of MPX_3 feature symmetry-protected valleys at the K and K' points, which can be manipulated by external fields to achieve valley polarization, highlighting their potential for valleytronic applications.

Furthermore, as shown in Figs. 2 and S2 [36], the contribution to the valence band maximum differs between the two material families. In contrast to the case of $MnPX_3$, where the valence band maximum is predominantly derived from the $4p$ orbitals of the nonmetal X atoms, in VPX_3 it primarily originates from the $3d$ orbitals of the transition metal V. Notably, d-p orbital hybridization is observed across all six materials, indicating the presence of superexchange interactions in these

TABLE I. Lattice constant a, band gap, and magnetic energy difference for MPX_3 in their magnetic ground states.

Materials[a]	a (Å)	Band gap (eV)	$\Delta E_{\mathrm{AFM-FM}}$ (meV/f.u.)
$\mathrm{MnPS_3}$	6.15 6.15*	2.54	–23.7
$\mathrm{MnPSe_3}$	6.47 6.39*	1.87	–16.5
$\mathrm{MnPTe_3}$	7.01 6.99*	0.91	–11.6
$\mathrm{VPS_3}$	5.99 5.85*	2.39	–154.9
$\mathrm{VPSe_3}$	6.34 6.24*	1.79	–108.1
$\mathrm{VPTe_3}$	6.86 6.98*	0.95	–68.0

[a] The data with * are from theoretical or experimental works [16,19,20,23,39,40].

systems [38]. In addition, due to the presence of P symmetry, the spin-up and spin-down bands remain strictly degenerate at every k-point in the Brillouin zone.

C. Thermodynamic and dynamical stability of adsorption structures

To evaluate the thermal stability of adsorption configurations at different coverages, we considered four coverages (25%, 50%, 75%, and 100%) for the $\mathrm{S_2}$ adsorption site. For the $\mathrm{S_1}$ and $\mathrm{S_3}$ sites, to ensure uniformity in the initial adsorption geometries, three coverages (25%, 50%, and 100%) were examined, as illustrated in Figs. S2 and S3 [36].

The stability of adsorption geometries and coverages is governed by the adsorbates' chemical potential, which can in turn modulate the intrinsic stability of the host lattice. We therefore first establish the stability window of the pristine hosts before addressing adsorption. In the case of MPX_3, to keep the host stable we have

$$\Delta\mu_{\mathrm{M}} + \Delta\mu_{\mathrm{P}} + 3\Delta\mu_{\mathrm{X}} = \Delta H_f(MPX_3), \tag{2}$$

where $\Delta H_f(MPX_3)$ is the formation enthalpy obtained from first-principles calculations. Here, $\Delta\mu_M$, $\Delta\mu_{\mathrm{P}}$, and $\Delta\mu_X$ represent the relative chemical potentials of elements M, P, and X with respect to their solid bulk phases (extreme rich limits), respectively. These chemical potentials depend on the experimental growth conditions and are treated as variables in the formalism. They are further constrained by the values that would lead to the precipitation of solid elemental M, P, and X, hence

$$\Delta\mu_{\mathrm{M}} \leqslant 0, \quad \Delta\mu_{\mathrm{P}} \leqslant 0, \quad \Delta\mu_{\mathrm{X}} \leqslant 0. \tag{3}$$

In addition, values that cause the precipitation of competing binary phases must also be considered. For $\mathrm{VPSe_3}$, the key constraints are

$$\Delta\mu_{\mathrm{P}} + \Delta\mu_{\mathrm{Se}} \leqslant \Delta H_f(\mathrm{PSe}), \tag{4}$$

$$\Delta\mu_{\mathrm{V}} + 2\Delta\mu_{\mathrm{Se}} \leqslant \Delta H_f(\mathrm{VSe_2}). \tag{5}$$

TABLE II. Adsorption energies E_{ad} (eV/atom) for O, F, and Be adatoms on monolayer $\mathrm{VPSe_3}$, $\mathrm{MnPS_3}$, and $\mathrm{VPS_3}$, respectively, across different coverage regimes. The adsorption site is S_3 for O and F adatoms, and S_1 for Be adatoms.

Coverage	25%	50%	75%	100%
$E_{\mathrm{ad}}(\mathrm{O})$	–3.22	–3.78	–3.77	–3.98
$E_{\mathrm{ad}}(\mathrm{F})$	–2.70	–2.82	–2.87	–2.94
$E_{\mathrm{ad}}(\mathrm{Be})$	–1.97	–2.43		–1.84

For $\mathrm{MnPS_3}$, the relevant constraints include

$$\Delta\mu_{\mathrm{Mn}} + \Delta\mu_{\mathrm{S}} \leqslant \Delta H_f(\mathrm{MnS}), \tag{6}$$

$$2\Delta\mu_{\mathrm{P}} + 5\Delta\mu_{\mathrm{S}} \leqslant \Delta H_f(\mathrm{P_2S_5}), \tag{7}$$

$$4\Delta\mu_{\mathrm{P}} + 5\Delta\mu_{\mathrm{S}} \leqslant \Delta H_f(\mathrm{P_4S_5}). \tag{8}$$

For $\mathrm{VPS_3}$, the corresponding constraints are as follows:

$$5\Delta\mu_{\mathrm{V}} + 8\Delta\mu_{\mathrm{P}} \leqslant \Delta H_f(\mathrm{V_5P_8}), \tag{9}$$

$$2\Delta\mu_{\mathrm{P}} + 7\Delta\mu_{\mathrm{S}} \leqslant \Delta H_f(\mathrm{P_2S_7}), \tag{10}$$

$$4\Delta\mu_{\mathrm{P}} + 7\Delta\mu_{\mathrm{S}} \leqslant \Delta H_f(\mathrm{P_4S_7}). \tag{11}$$

The range of $\Delta\mu_{\mathrm{V}}$, $\Delta\mu_{\mathrm{P}}$, and $\Delta\mu_{\mathrm{Se}}$ that satisfies Eqs. (2)–(5) defines the thermodynamic stability region of $\mathrm{VPSe_3}$, while the range of $\Delta\mu_{\mathrm{Mn}}$, $\Delta\mu_{\mathrm{P}}$, and $\Delta\mu_{\mathrm{Se}}$ satisfying Eqs. (2), (3), and (6)–(8) defines that of $\mathrm{MnPS_3}$. These regions suggest possible equilibrium experimental growth conditions. For $\mathrm{VPS_3}$, the corresponding range of $\Delta\mu_{\mathrm{V}}$, $\Delta\mu_{\mathrm{P}}$, and $\Delta\mu_{\mathrm{S}}$ that fulfills Eqs. (2), (3), and (9)–(11) determines its thermodynamic stability region, which was previously computed in our earlier work [41]. No solution to these equations implies that the studied material is thermodynamically unstable, and its experimental synthesis under equilibrium conditions would be challenging or unfeasible, since kinetic barriers between different phases are often negligible or surmountable at elevated temperatures.

The calculated chemical potential phase diagrams for $\mathrm{VPSe_3}$, $\mathrm{MnPS_3}$, and $\mathrm{VPS_3}$ are presented in Figs. 3(a), 3(b), and 3(c), respectively. The light blue regions denote the allowed ranges of chemical potentials, confirming the thermodynamic stability of these compounds. In addition, we computed the thermodynamic phase diagram of $\mathrm{MnPTe_3}$. Our results reveal that, in contrast, $\mathrm{MnPTe_3}$ is thermodynamically unstable, as the stability region of the competing binary phase MnTe completely encompasses the entire region where the ternary phase would otherwise be stable, thereby precluding its stabilization. This finding is consistent with experimental observations: while $\mathrm{MnPS_3}$ and $\mathrm{VPS_3}$ have been successfully synthesized, no reports on the synthesis of $\mathrm{MnPTe_3}$ exist in the literature [42,43]. Nevertheless, $\mathrm{MnPTe_3}$ may still be attainable as a metastable phase through nonequilibrium synthesis techniques.

Additionally, the calculated adsorption energies at different coverages are summarized in Table II. Since the adsorption

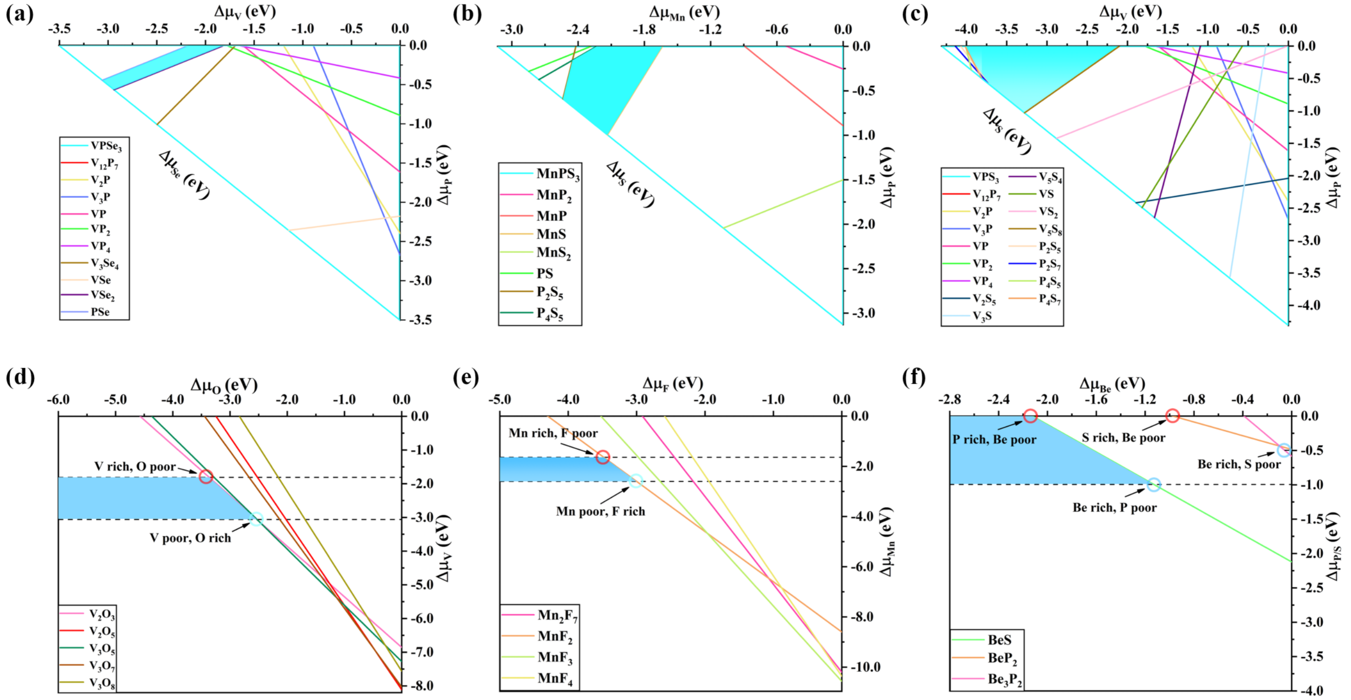

FIG. 3. (a) Phase stability diagram of $VPSe_3$ projected onto the $(\Delta\mu_V, \Delta\mu_P)$ plane. The blue region represents the thermodynamically allowed range of V, P, and Se chemical potentials under equilibrium conditions. (b) Phase stability diagram of $MnPS_3$ projected onto the $(\Delta\mu_{Mn}, \Delta\mu_P)$ plane. The blue region indicates the range of Mn, P, and S chemical potentials allowed under thermodynamic equilibrium. (c) Phase stability diagram of VPS_3 projected onto the $(\Delta\mu_V, \Delta\mu_P)$ plane. The blue region represents the thermodynamically allowed range of V, P, and S chemical potentials under equilibrium conditions. (d) V-O phase diagram constrained by the permissible range of $\Delta\mu_V$. The blue region corresponds to the stable range of oxygen chemical potential $\Delta\mu_O$. (e) Mn-F phase diagram constrained by the permissible range of $\Delta\mu_{Mn}$. The blue region corresponds to the stable range of fluorine chemical potential $\Delta\mu_F$. (f) Be-P-S phase diagram constrained by the permissible ranges of $\Delta\mu_P$ and $\Delta\mu_S$. The blue region defines the stable range of beryllium chemical potential $\Delta\mu_{Be}$.

energy E_{ad} is directly related to the chemical potential $\Delta\mu$ of the adsorbate, a comparison of coverage-dependent chemical potentials with the corresponding stability boundaries reveals the following. As shown in Figs. 3(d)–3(f), under P-rich and Be-poor conditions, Be_xVPS_3 is thermodynamically stable only at 50% coverage, whereas under P-rich and Be-rich conditions, it remains stable for all three coverages considered. For $VPSe_3O_x$, adsorption at 25% coverage is stable exclusively under V-poor and O-rich conditions, while configurations with other coverages are thermodynamically stable across the entire range of chemical potentials studied. For $MnPS_3F_x$, the 100% coverage structure is thermodynamically stable only under Mn-poor and F-rich conditions; under Mn-rich and F-poor conditions, all coverage configurations are thermodynamically unstable. Furthermore, the coverage-dependent adsorption energies indicate that higher coverage configurations are energetically more favorable for $VPSe_3O_x$ and $MnPS_3F_x$, whereas for Be_xVPS_3, the 50% coverage configuration is the most energetically preferred. To assess their dynamical stability, the phonon spectra of these three structures were calculated, as shown in Fig. S5 [36]. The absence of appreciable imaginary frequencies confirms that they are dynamically stable. Therefore, in the following analysis, we focus on the electronic and magnetic properties of the higher-coverage adsorption structures—namely, $VPSe_3O_{0.5}$, $MnPS_3F_{0.5}$, and $Be_{0.5}VPS_3$.

D. O atom adsorption unlock altermagnetism in $VPSe_3$

Upon O adsorption, the magnetic configuration of $VPSe_3$ remains unchanged, with the energy difference between AFM and FM states, $\Delta E_{\text{AFM-FM}}$, being –23.4 meV/f.u., as shown in Table III. We computed the charge density difference for $VPSe_3$ after O adsorption [see Fig. 4(a)], and the electron transfer before and after adsorption was further analyzed using Bader charge calculations. In the plot, the yellow regions around O represent electron accumulation, while the blue regions around P indicate electron depletion. As shown in Fig. S6(a) [36], the calculated electron localization function (ELF) of the adsorption structures reveals that the bonding between the adsorbed O atom and the surface P atoms is predominantly ionic. Upon O adsorption, electrons are transferred from $VPSe_3$ to O by 0.63 electrons, leading to a

TABLE III. Bader charge transfer, and magnetic energy difference $\Delta E_{\text{AFM-FM}}$ for the adsorption of O and F at 100% and Be adatoms at 50% coverage on monolayer $VPSe_3$, $MnPS_3$, and VPS_3, respectively.

Materials	$VPSe_3O_{0.5}$	$MnPS_3F_{0.5}$	$Be_{0.5}VPS_3$
Bader charge (e/f.u.)	0.63	0.36	–0.79
$\Delta E_{\text{AFM-FM}}$ (meV/f.u.)	–23.4	20.6	–43.1

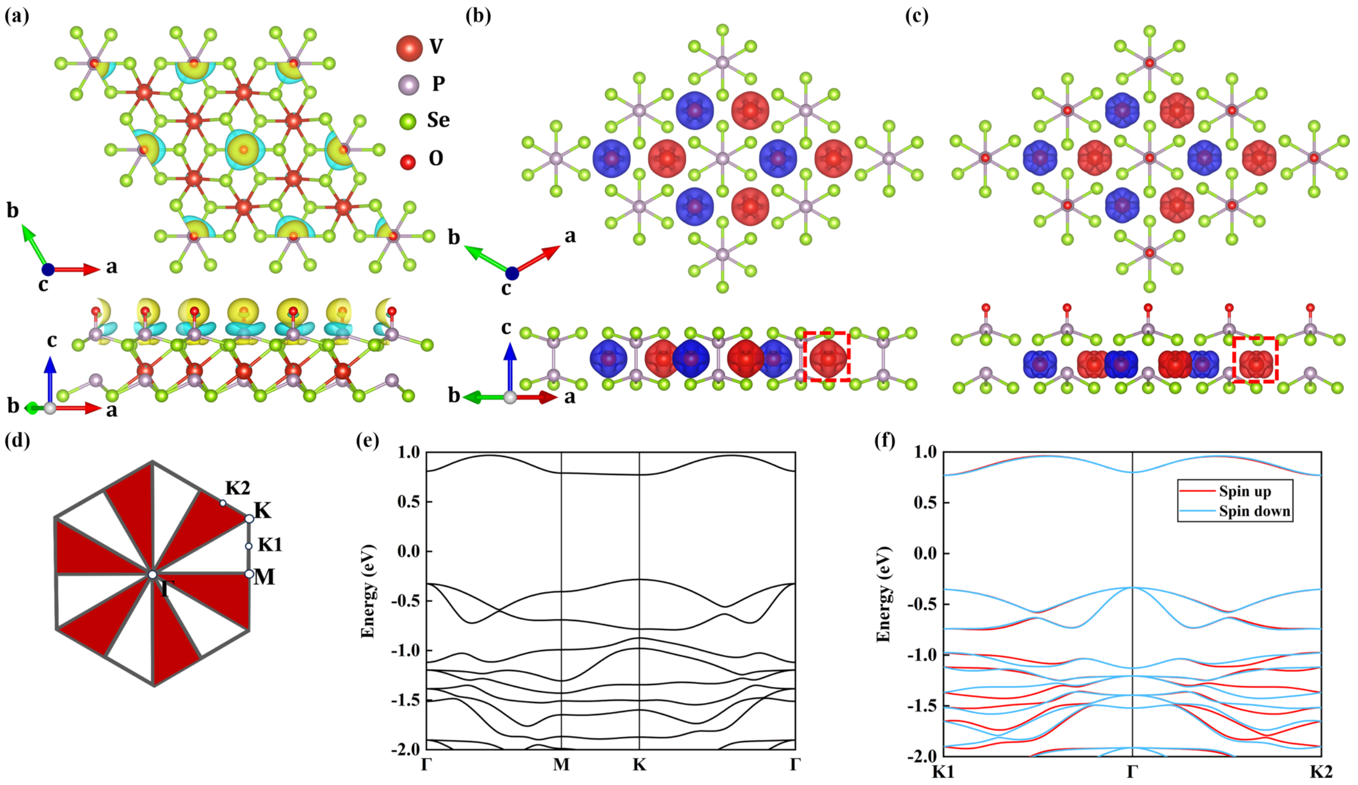

FIG. 4. (a) Charge density difference of $VPSe_3$ after O adsorption, where blue and yellow distributions correspond to the charge depletion and accumulation, respectively. (b) and (c) show the spin density of $VPSe_3$ before and after O adsorption, respectively, with red and blue regions indicating spin-up and spin-down densities. (d) Resulting alternating spin polarization in momentum space after O adsorption. Spin-polarized band structures along (e) the high-symmetry path Γ-M-K-Γ and (f) the non-high-symmetry path $K1$-Γ-$K2$.

reduction in the band gap. Notably, the charge redistribution induced by adsorption also causes significant changes in the spin density. As shown in Figs. 4(b) and 4(c), we plotted the spin density distributions of $VPSe_3$ before and after adsorption. The side view reveals a dramatic reshaping of the spin density after adsorption, further reflecting the symmetry breaking introduced by the adsorbate.

We also plotted the band structures along different high-symmetry paths, as shown in Figs. 4(e) and 4(f). Along the $K1$-Γ-$K2$ path, the spin-up and spin-down bands split in a symmetric manner with respect to the k points, whereas along the high symmetry path Γ-M-K-Γ, they remain strictly degenerate, indicating a strong momentum dependence of the spin splitting. Remarkably, the magnitude of the spin splitting reaches 112.4 meV, significantly larger than those reported in many other 2D AMs, such as $MnPSe_3$ under an electric field (25 meV), $MnP(S,Se)_3$ (100 meV), and $PtBr_3$ in an inverted stacking configuration (18 meV) [22,44]. This spin splitting can be understood from a symmetry perspective: the introduced adsorbate breaks the P symmetry, thereby lifting the Kramer's spin degeneracy. However, the spin-up and spin-down bands remain constrained by the $[C_2\|m]$ symmetry operation, resulting in alternating spin splitting while maintaining a net zero magnetic moment in the system.

To validate the effectiveness of this approach, we further computed the case of O adsorption on the $VPTe_3$ surface, as presented in the Fig. S7 [36]. Similarly, nonrelativistic alternating spin splitting emerges along the non-high-symmetry path $K1$-Γ-$K2$ after adsorption, with a splitting value of 121.1 meV, while the bands remain strictly spin-degenerate along high-symmetry directions. In contrast to $VPSe_3$, where the adsorption-induced spin splitting occurs mainly in the valence bands near the Fermi level, the spin splitting in $VPTe_3$ is more pronounced in the conduction bands. These results demonstrate that surface adsorption serves as an effective approach to unlocking altermagnetism in VPX_3 materials.

E. F atom adsorption induced AFM-FM transition in $MnPS_3$

Interestingly, in $MnPX_3$, we observe that the adsorption of elements with strong oxidizing capability (O and F atom) can induce an AFM-FM magnetic phase transition. This finding is consistent with previous studies reporting that magnetic phase transitions in MPX_3 can be triggered by charge doping or biaxial strain [19]. We systematically investigated the adsorption of O and F atoms on $MnPS_3$ and $MnPTe_3$ surfaces (Figs. S8–S10) [36]. Among the four resulting configurations, only O-adsorbed $MnPS_3$ retains a band gap. Notably, this structure does not undergo AFM-FM transition. In the other three cases, at full coverage, adsorption drives the system to transition from a semiconductor to either a metal or a half-metal, accompanied by an AFM-FM magnetic transition. The relative energies of different magnetic configurations for $MnPS_3$ and $MnPTe_3$ upon adsorption of O and F atoms are summarized in Table S2 [36]. To elucidate the origin of the magnetic phase transition, we focus on the electronic and magnetic modifications induced by F adsorption on $MnPS_3$.

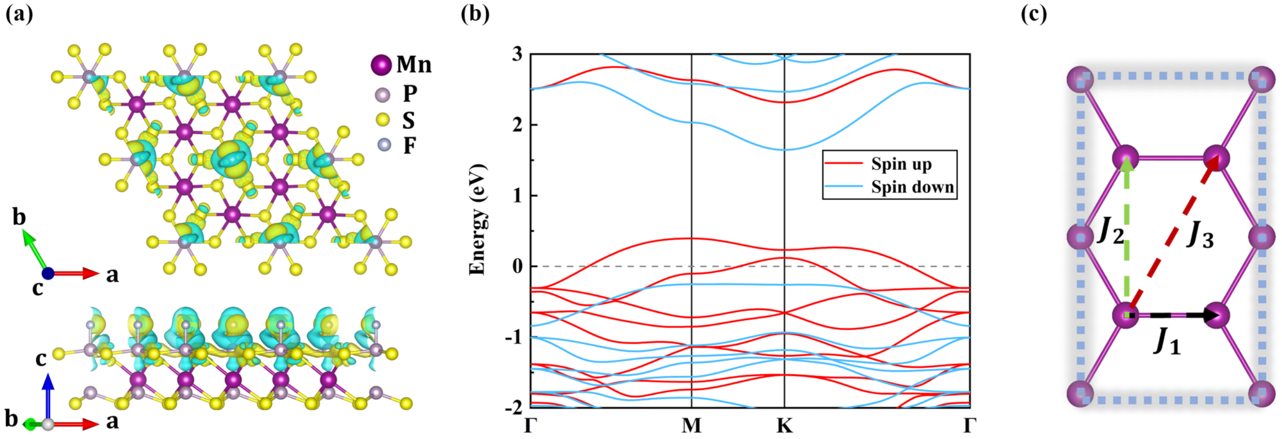

FIG. 5. (a) Differential charge density of $MnPS_3$ after F atom adsorption, and (b) the corresponding spin-polarized band structure. (c) Magnetic exchange parameters J_1, J_2, and J_3 between Mn^{2+} ions. The blue and yellow distributions correspond to the charge depletion and accumulation, respectively.

After adsorption, the energy difference between the AFM and FM states of $MnPS_3$ becomes 20.6 meV/f.u., indicating the occurrence of an AFM-FM magnetic phase transition (see Table III). The differential charge density plot after adsorption is shown in Fig. 5(a). Here, as shown in Fig. S6(b) [36], a clear bonding feature between the adsorbed F atom and the surface P atom is observed. The bond is predominantly ionic, leading to a charge transfer of 0.36 e/f.u. from $MnPS_3$ to the F atom. Figure 5(b) presents the spin-polarized band structure of the adsorbed system. F adsorption transforms $MnPS_3$ from a semiconductor into a half-metal, with significant spin splitting emerging in the valence band.

To better describe the 2D magnetic structure, we recast the system in terms of an effective Heisenberg Hamiltonian:

$$H = \sum_{\langle i,j\rangle} J_1 \vec{S}_i \cdot \vec{S}_j + \sum_{\langle\langle i,j\rangle\rangle} J_2 \vec{S}_i \cdot \vec{S}_j + \sum_{\langle\langle\langle i,j\rangle\rangle\rangle} J_3 \vec{S}_i \cdot \vec{S}_j, \quad (12)$$

where $\vec{S}_i$ represents the total spin magnetic moment at atomic site i, and J_1, J_2, and J_3 denote the exchange interactions between the first, second, and third nearest-neighbor spins, respectively, as illustrated in Fig. 5(c). In the pristine monolayer $MnPS_3$, all calculated exchange constants J are positive, indicating the dominance of AFM exchange interactions, with values $J_1 = 0.56$ meV, $J_2 = 0.04$ meV, and $J_3 = 0.19$ meV. In contrast, the magnitude of J_2 is substantially smaller than those of J_1 and J_3, consistent with previous studies [29]. The negative J_1 arises from a competition between direct exchange and superexchange. Direct exchange originates from hopping between nearest-neighbor Mn ions, where overlapping half-filled 3d orbitals provide a stable AFM state. Meanwhile, according to the Goodenough-Kanamori-Anderson (GKA) rules, the superexchange interaction is FM due to the Mn-S-Mn bond angle of 83.54° [45]. However, given the high-spin state of the Mn ions in monolayer $MnPS_3$, the direct AFM interaction dominates over the FM superexchange.

For J_2 and J_3, the AFM exchange arises from super-superexchange interactions mediated by different S atoms. Specifically, J_2 involves a Mn-S3···S6-Mn path, in which the two S atoms reside in separate sublayers (Fig. S11 [36]). In contrast, for the super-super-exchange channel of J_3, the two mediating S atoms lie within the same sublayer (Mn-S1···S2-Mn). It is reasonable to expect that the hybridization of Mn d states with S p states within the same sublayer is considerably stronger than that between different sublayers. This accounts for the larger magnitude of J_3 compared to J_2, despite the longer Mn-Mn distance in the former case. Nonetheless, J_1 remains three times larger than J_3, establishing the direct Mn-Mn AFM exchange as the dominant interaction in the pristine $MnPS_3$ monolayer.

Upon F atom adsorption, the exchange parameters of $MnPS_3$ exhibit pronounced changes. Specifically, the adsorption results in $J_1 = -0.32$ meV, $J_2 = -0.34$ meV, and $J_3 = -0.39$ meV, indicating a complete transition from the original AFM coupling to FM coupling. The magnetic moment of the Mn ions changes from 4.60 μ_B to 4.56 μ_B after adsorption. Although the Mn-Mn distances remain nearly unchanged, F adsorption increases the Mn-S-Mn bond angle on one side to 85.91° and reduces the Mn-S bond length. More importantly, the adsorption induces the disappearance of the band gap in $MnPS_3$, thereby enhancing the Mn-S-Mn superexchange interaction. This effect reverses the dominance of J_1 and triggers an AFM-FM transition.

F. Realization of fFIM phase in VPS_3 via Be atom adsorption

Furthermore, we find that adsorption can readily induce FIM order in MPX_3. Symmetry analysis reveals that as long as the adsorbed atoms break all symmetry operations connecting the two spin sublattices, ferrimagnetism emerges in MPX_3 in the absence of AFM-FM transition. Among the three adsorption sites, only the S_1 site lies on no symmetry element; it is also generally the most energetically favorable site for metal atom adsorption. Notably, if metal atoms are adsorbed at both S_1 sites of the two spin sublattices—corresponding to 100% coverage—the mirror symmetry m of MPX_3 is preserved, and the system exhibits altermagnetism (see Fig. S12(d) [36]). Based on these considerations, we demonstrate here that adsorption of metal atoms can induce FIM in MPX_3.

In FM/FIM semiconductors, insulators, and half-metals, the magnetic moment per primitive cell must be an integer

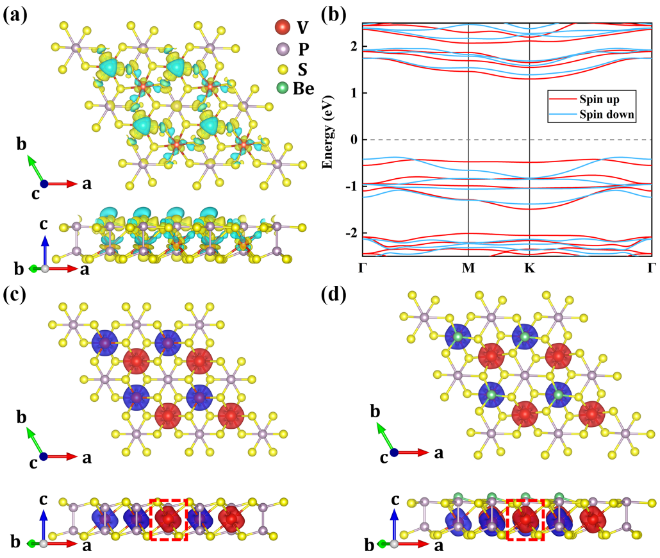

FIG. 6. (a) Differential charge density of VPS_3 after Be atom adsorption, and (b) the corresponding electronic band structure. Spin density of VPS_3 (c) before and (d) after Be atom adsorption, with red and blue regions indicating spin-up and spin-down densities. The blue and yellow distributions correspond to the charge depletion and accumulation, respectively.

multiple of the Bohr magneton, i.e., 0, 1, 2 μ_B, etc. This arises because the net magnetization in a typical ferromagnet/ferrimagnet is given by

$$M = \mu_B(N_\uparrow - N_\downarrow), \quad (13)$$

where μ_B is the Bohr magneton, and $N_\uparrow$ and $N_\downarrow$ denote the number of occupied states in the spin-up and spin-down channels, respectively. If a band gap exists in one spin channel, regardless of the other, the net magnetization must be an integer multiple of μ_B. Consequently, when the total magnetization is zero, it is strictly zero at $T = 0$ K.

Taking the adsorption of Be atoms on a monolayer VPS_3 surface as an example, the energy difference between the AFM and FM configurations is calculated to be –43.1 meV/f.u., as shown in Table III. The corresponding differential charge density plot [Fig. 6(a)] reveals a significant redistribution of electrons at the adsorption interface. As shown in Fig. S6(c) [36], the calculated ELF reveals that the bonding between the Be atom and the surface S atoms is predominantly covalent. According to Bader charge analysis, each Be atom transfers 0.79e to the VPS_3 substrate. The spin-polarized band structure of this system in the AFM state is shown in Fig. 6(b). A pronounced spin splitting is observed along the high-symmetry directions. To understand the origin of this behavior, we further examine the spin density distributions of the monolayer VPS_3 before and after Be adsorption [Figs. 6(c) and 6(d)]. Prior to adsorption, the spin-up and spin-down electron densities are uniformly and symmetrically distributed. After Be adsorption, however, the spin-down electron density shifts, breaking the symmetry relation between the two spin sublattices. This symmetry breaking induces an FM-like spin splitting in the electronic bands. It is noteworthy that the system remains semiconducting and possesses zero net magnetic moment. Such a compensated semiconducting system, exhibiting spin-split bands with a net magnetization, is classified as a "Luttinger-compensated" ferrimagnet [46].

Similarly, we investigated the adsorption of Be and Ca atoms on $MnPSe_3$ to achieve a fFIM state (Figs. S12 and S13 [36]). However, the Ca-adsorbed system favors a ZAFM order, with an energy difference of –1.04 meV/f.u. relative to the NAFM configuration. Since the ZAFM order in $MnPSe_3$ corresponds to a $T\tau$-type antiferromagnet, and the highest coverage of Ca adsorption cannot break the symmetry protecting the spin degeneracy, the system retains spin-degenerate bands even at maximum Ca coverage. Nevertheless, the NAFM state exists as a metastable phase with a very small energy difference from the ZAFM state. The band structure of this metastable state exhibits spin splitting while maintaining zero total magnetic moment per unit cell. Given the finite band gap, the net magnetization remains strictly zero in theory.

IV. DISCUSSION

According to the Mermin-Wagner theorem, long-range magnetic order cannot exist in 2D isotropic systems at finite temperatures due to thermal fluctuations [47]. Consequently, magnetic anisotropy arising from spin-orbit coupling (SOC) plays a crucial role in stabilizing long-range magnetic order in 2D materials. The magnetic anisotropy energy (MAE) was defined as MAE $= E[100] - E[001]$. We evaluated the MAE for pristine $VPSe_3$, $MnPS_3$, and VPS_3, as well as for their corresponding adsorption structures $VPS_3O_{0.5}$, $MnPS_3F_{0.5}$, and $Be_{0.5}VPS_3$. For the first five structures, owing to their relatively high symmetry, the MAE was calculated with the easy axis aligned along the [100], [010], and [001] directions. For $Be_{0.5}VPS_3$, which possesses the lowest symmetry among the systems considered, additional calculations were performed with the easy axis oriented along the [110], [210], and [120] directions. The computed MAE values are summarized in Table S3. Notably, the out-of-plane easy axis of pristine $VPSe_3$ switches to an in-plane orientation upon oxygen adsorption, indicating that atomic adsorption provides an effective means to manipulate the direction of the magnetic easy axis. Furthermore, for the fully compensated ferrimagnetic system $Be_{0.5}VPS_3$, the inclusion of spin-orbit coupling yields a net magnetic moment of approximately 0.003 μ_B/f.u.

To assess the robustness of our qualitative conclusions with respect to the choice of Hubbard U parameters, we performed additional calculations using different U values for the three representative materials presented in the main text, namely $VPSe_3$, $MnPS_3$, and VPS_3, both before and after adsorption. Specifically, for V, we tested $U = 2$, 3.25, and 4 eV, while for Mn we considered $U = 3$, 4, and 5 eV. As summarized in Ref. [36] (Tables S4–S9), the magnetic ground states remain unchanged across the tested U range for all structures. This indicates that our key findings—particularly the adsorption-induced magnetic phase transitions—are not sensitive to the specific choice of U within reasonable bounds, thereby reinforcing the reliability of our conclusions.

The calculated Néel temperatures of pristine $VPSe_3$, $MnPS_3$, and VPS_3 are shown in Fig. S14 [36], with values of approximately 300, 90, and 360 K, respectively. Upon adsorption of O and Be atoms, the Néel temperatures of $VPSe_3$ and VPS_3 decrease to about 50 and 95 K, respectively.

Notably, F adsorption raises the Curie temperature of $MnPS_3$ to approximately 225 K.

V. CONCLUSION

In summary, our first-principles calculations confirm that surface adsorption serves as an effective strategy for tailoring the magnetic properties of monolayer MPX_3. For the VPX_3 systems, adsorption of highly electronegative elements such as O, F, and Cl unlocks a hidden AM phase. In the case of $MnPX_3$, the adsorption of such atoms not only induces a semiconductor-to-half-metal transition but also triggers an AFM-FM magnetic phase transition. More importantly, the adsorption of metallic elements effectively breaks the symmetry connecting opposite magnetic sublattices, thereby inducing a FIM order in MPX_3 and achieving a fFIM state while preserving the electronic band gap. Taking $VPSe_3$, $MnPS_3$, and VPS_3 as representative examples, we demonstrate that adsorption of different atomic species can stabilize AM, FM, and fFIM states, respectively. Furthermore, analysis of the thermodynamic phase diagram and phonon spectra confirms that these three adsorption configurations exhibit favorable thermodynamic and dynamical stability under high coverage conditions. Through systematic analysis of the changes in magnetic and electronic properties before and after adsorption, we verify the reliability of this tuning approach. Our study not only deepens the understanding of surface-adsorption-mediated control over the electronic and magnetic properties of MPX_3, but also provides a theoretical foundation for the design of tunable spintronic devices based on MPX_3 and related structures.

ACKNOWLEDGMENTS

This work was supported by the Guangdong Basic and Applied Basic Research Foundation (No. 2023A1515012289) and the National Natural Science Foundation of China (Grant No. 12474229). This work is partially supported by High Performance Computing Platform of South China University of Technology.

DATA AVAILABILITY

The data that support the findings of this article are not publicly available. The data are available from the authors upon reasonable request.

[1] V. Baltz, A. Manchon, M. Tsoi, T. Moriyama, T. Ono, and Y. Tserkovnyak, Antiferromagnetic spintronics, Rev. Mod. Phys. **90**, 015005 (2018).

[2] L. Šmejkal, J. Sinova, and T. Jungwirth, Beyond conventional ferromagnetism and antiferromagnetism: A phase with nonrelativistic spin and crystal rotation symmetry, Phys. Rev. X **12**, 031042 (2022).

[3] L. Šmejkal, R. González-Hernández, T. Jungwirth, and J. Sinova, Crystal time-reversal symmetry breaking and spontaneous Hall effect in collinear antiferromagnets, Sci. Adv. **6**, eaaz8809 (2020).

[4] L. Šmejkal, A. H. MacDonald, J. Sinova, S. Nakatsuji, and T. Jungwirth, Anomalous Hall antiferromagnets, Nat. Rev. Mater. **7**, 482 (2022).

[5] K. Samanta, M. Ležaić, M. Merte, F. Freimuth, S. Blügel, and Y. Mokrousov, Crystal Hall and crystal magneto-optical effect in thin films of $SrRuO_3$, J. Appl. Phys. **127**, 213904 (2020).

[6] X. Zhou, W. Feng, X. Yang, G.-Y. Guo, and Y. Yao, Crystal chirality magneto-optical effects in collinear antiferromagnets, Phys. Rev. B **104**, 024401 (2021).

[7] Z. Jin, Z. Zeng, Y. Cao, and P. Yan, Skyrmion Hall effect in altermagnets, Phys. Rev. Lett. **133**, 196701 (2024).

[8] X. Zhou, W. Feng, R.-W. Zhang, L. Šmejkal, J. Sinova, Y. Mokrousov, and Y. Yao, Crystal thermal transport in altermagnetic RuO_2, Phys. Rev. Lett. **132**, 056701 (2024).

[9] L. Šmejkal, A. B. Hellenes, R. González-Hernández, J. Sinova, and T. Jungwirth, Giant and tunneling magnetoresistance in unconventional collinear antiferromagnets with nonrelativistic spin-momentum coupling, Phys. Rev. X **12**, 011028 (2022).

[10] M. Naka, S. Hayami, H. Kusunose, Y. Yanagi, Y. Motome, and H. Seo, Spin current generation in organic antiferromagnets, Nat. Commun. **10**, 4305 (2019).

[11] M. Naka, Y. Motome, and H. Seo, Perovskite as a spin current generator, Phys. Rev. B **103**, 125114 (2021).

[12] R. González-Hernández, L. Šmejkal, K. Výborný, Y. Yahagi, J. Sinova, T. Jungwirth, and J. Železný, Efficient electrical spin splitter based on nonrelativistic collinear antiferromagnetism, Phys. Rev. Lett. **126**, 127701 (2021).

[13] Y. Liu, S.-D. Guo, Y. Li, and C.-C. Liu, Two-dimensional fully compensated ferrimagnetism, Phys. Rev. Lett. **134**, 116703 (2025).

[14] B. Huang, G. Clark, E. Navarro-Moratalla, D. R. Klein, R. Cheng, K. L. Seyler, D. Zhong, E. Schmidgall, M. A. McGuire, D. H. Cobden, W. Yao, D. Xiao, P. Jarillo-Herrero, and X. Xu, Layer-dependent ferromagnetism in a van der Waals crystal down to the monolayer limit, Nature (London) **546**, 270 (2017).

[15] C. Gong, L. Li, Z. Li, H. Ji, A. Stern, Y. Xia, T. Cao, W. Bao, C. Wang, Y. Wang, Z. Q. Qiu, R. J. Cava, S. G. Louie, J. Xia, and X. Zhang, Discovery of intrinsic ferromagnetism in two-dimensional van der Waals crystals, Nature (London) **546**, 265 (2017).

[16] A. Wiedenmann, J. Rossat-Mignod, A. Louisy, R. Brec, and J. Rouxel, Neutron diffraction study of the layered compounds $MnPSe_3$ and $FePSe_3$, Solid State Commun. **40**, 1067 (1981).

[17] J. Tan, H. Hu, B. Cai, D. Xu, and G. Ouyang, Instability of the magnetic state of MPX_3 ($M =$ Mn, Ni; $X =$ S, Se) monolayers induced by strain and doping, Phys. Rev. B **106**, 195424 (2022).

[18] X. Li, X. Wu, and J. Yang, Half-metallicity in $MnPSe_3$ exfoliated nanosheet with carrier doping, J. Am. Chem. Soc. **136**, 11065 (2014).

[19] B. L. Chittari, Y. Park, D. Lee, M. Han, A. H. MacDonald, E. Hwang, and J. Jung, Electronic and magnetic properties of single-layer MPX_3 metal phosphorous trichalcogenides, Phys. Rev. B **94**, 184428 (2016).

[20] Y. Gao, X. Jiang, Z. Qiu, and J. Zhao, Photoexcitation induced magnetic phase transition and spin dynamics in antiferromagnetic $MnPS_3$ monolayer, npj Comput. Mater. **9**, 107 (2023).

[21] D. Liu, S. Zeng, J.-H. Liao, and Y.-J. Zhao, Tuning electronic and magnetic properties of monolayer $MnPSe_3$ via surface adsorption, J. Phys. Chem. C **129**, 17287 (2025).

[22] I. Mazin, R. González-Hernández, and L. Šmejkal, Induced monolayer altermagnetism in $MnP(S, Se)_3$ and FeSe, arXiv:2309.02355.

[23] H. Sun, P. Dong, C. Wu, and P. Li, Multifield-induced antiferromagnet transformation into altermagnet and realized anomalous valley Hall effect in monolayer $VPSe_3$, Phys. Rev. B **111**, 235431 (2025).

[24] X.-J. Dong, K. Jia, W.-X. Ji, S.-S. Li, and C.-W. Zhang, Realization of dual anomalous valley Hall effect in antiferromagnetic $HfN_2/MnPSe_3$ heterostructure, ACS Appl. Electron. Mater. **6**, 679 (2024).

[25] C. Zhang, H. Pi, and J. Zhou, Bulk photovoltaic effects in helimagnets, Phys. Rev. B **110**, L041104 (2024).

[26] J. P. Perdew, K. Burke, and M. Ernzerhof, Generalized gradient approximation made simple, Phys. Rev. Lett. **77**, 3865 (1996).

[27] G. Kresse and J. Furthmüller, Efficient iterative schemes for ab initio total-energy calculations using a plane-wave basis set, Phys. Rev. B **54**, 11169 (1996).

[28] X. Wang, D.-S. Wang, R. Wu, and A. J. Freeman, Validity of the force theorem for magnetocrystalline anisotropy, J. Magn. Magn. Mater. **159**, 337 (1996).

[29] N. Sivadas, M. W. Daniels, R. H. Swendsen, S. Okamoto, and D. Xiao, Magnetic ground state of semiconducting transition-metal trichalcogenide monolayers, Phys. Rev. B **91**, 235425 (2015).

[30] X.-Q. Han, P.-J. Guo, Z.-F. Gao, and Z.-Y. Lu, PhononBench: A large-scale phonon-based benchmark for dynamical stability in crystal generation, arXiv:2512.21227.

[31] X.-Q. Han, P.-J. Guo, Z.-F. Gao, H. Sun, and Z.-Y. Lu, InvDesFlow-AL: Active learning-based workflow for inverse design of functional materials, npj Comput. Mater. **11**, 364 (2025).

[32] X.-Q. Han, Z. Ouyang, P.-J. Guo, H. Sun, Z.-F. Gao, and Z.-Y. Lu, InvDesFlow: An AI-driven materials inverse design workflow to explore possible high-temperature superconductors, Chin. Phys. Lett. **42**, 047301 (2025).

[33] X.-Q. Han, X.-D. Wang, M.-Y. Xu, Z. Feng, B.-W. Yao, P.-J. Guo, Z.-F. Gao, and Z.-Y. Lu, AI-driven inverse design of materials: Past, present, and future, Chin. Phys. Lett. **42**, 027403 (2025).

[34] N. Bazazzadeh, M. Hamdi, F. Haddadi, A. Khavasi, A. Sadeghi, and S. M. Mohseni, Symmetry enhanced spin-Nernst effect in honeycomb antiferromagnetic transition metal trichalcogenide monolayers, Phys. Rev. B **103**, 014425 (2021).

[35] R. F. L. Evans, W. J. Fan, P. Chureemart, T. A. Ostler, M. O. A. Ellis, and R. W. Chantrell, Atomistic spin model simulations of magnetic nanomaterials, J. Phys.: Condens. Matter **26**, 103202 (2014).

[36] See Supplemental Material at http://link.aps.org/supplemental/10.1103/lgdz-961s for the four magnetic configurations considered for pristine MPX_3 and their corresponding energy differences, the surface adsorption configurations with different coverages, the phonon spectra, electron localization functions, magnetic anisotropy energies, and Curie/Néel temperatures of $MnPS_3F_{0.5}$, $VPSe_3O_{0.5}$, and $Be_{0.5}VPS_3$, the energies of the four magnetic configurations under different Hubbard U values, as well as additional examples of surface-adsorption-induced altermagnetism, ferromagnetism, and fully compensated ferrimagnetism in MPX_3.

[37] S. Zeng and Y.-J. Zhao, Description of two-dimensional altermagnetism: Categorization using spin group theory, Phys. Rev. B **110**, 054406 (2024).

[38] S. Y. Kim, T. Y. Kim, L. J. Sandilands, S. Sinn, M.-C. Lee, J. Son, S. Lee, K.-Y. Choi, W. Kim, B.-G. Park, C. Jeon, H.-D. Kim, C.-H. Park, J.-G. Park, S. J. Moon, and T. W. Noh, Charge-spin correlation in van der Waals antiferromagnet $NiPS_3$, Phys. Rev. Lett. **120**, 136402 (2018).

[39] W. Zhou, G. Zheng, A. Li, D. Zhang, and F. Ouyang, Orbital contribution to the regulation of the spin-valley coupling in antiferromagnetic monolayer $MnPTe_3$, Phys. Rev. B **107**, 035139 (2023).

[40] W. Klingen, G. Eulenberger, and H. S. Hahn, Über hexachalkogeno-hypodiphosphate vom typ $M_2P_2X_6$, Naturwissenschaften **57**, 88 (1970).

[41] D. Liu, S. Zeng, J.-H. Liao, and Y.-J. Zhao, Unlocking altermagnetism in antiferromagnetic 2D films via adsorption, arXiv:2507.09518.

[42] G. Ouvrard, R. Brec, and J. Rouxel, Structural determination of some $MnPS_3$ layered phases ($M = $ Mn, Fe, Co, Ni and Cd), Mater. Res. Bull. **20**, 1181 (1985).

[43] G. Le Flem, R. Brec, G. Ouvard, A. Louisy, and P. Segransan, Magnetic interactions in the layer compounds MPX_3 ($M = $ Mn, Fe, Ni; $X = $ S, Se), J. Phys. Chem. Solids **43**, 455 (1982).

[44] W. Sun, H. Ye, L. Liang, N. Ding, S. Dong, and S.-S. Wang, Stacking-dependent ferroicity of a reversed bilayer: Altermagnetism or ferroelectricity, Phys. Rev. B **110**, 224418 (2024).

[45] J. Kanamori, Superexchange interaction and symmetry properties of electron orbitals, J. Phys. Chem. Solids **10**, 87 (1959).

[46] I. Mazin, Editorial: Altermagnetism—A new punch line of fundamental magnetism, Phys. Rev. X **12**, 040002 (2022).

[47] N. D. Mermin and H. Wagner, Absence of ferromagnetism or antiferromagnetism in one- or two-dimensional isotropic Heisenberg models, Phys. Rev. Lett. **17**, 1133 (1966).